frontiers in Physics

ORIGINAL RESEARCH
published: 28 January 2020
doi: 10.3389/fphy.2019.00232

$MAPbBr_{3-x}I_x$ Crystals Improved by Accurate Solution-Grown Procedure for Alpha Particle Detection

Xin Liu[1,2,3†], Jinghua Fu[2,3], Dou Zhao[2,3], Yingying Hao[2,3], Hao Zhu[2,3], Meng Xu[2,3], Binbin Zhang[2,3†], Wanqi Jie[1,2,3] and Yadong Xu[1,2,3†]*

[1] State Key Laboratory of Solidification Processing, Northwestern Polytechnical University, Xi'an, China, [2] Key Laboratory of Radiation Detection Materials and Devices of MIIT, Northwestern Polytechnical University, Xi'an, China, [3] School of Materials Science and Engineering, Northwestern Polytechnical University, Xi'an, China

OPEN ACCESS

Edited by:
Paul Sellin,
University of Surrey, United Kingdom

Reviewed by:
Ge Yang,
North Carolina State University, United States
Peter R. Hobson,
Queen Mary University of London, United Kingdom

***Correspondence:**
Yadong Xu
xyd220@nwpu.edu.cn

†ORCID:
Xin Liu
orcid.org/0000-0002-0409-1718
Binbin Zhang
orcid.org/0000-0002-1874-1881
Yadong Xu
orcid.org/0000-0002-1017-9337

Specialty section:
This article was submitted to Radiation Detectors and Imaging, a section of the journal Frontiers in Physics

Received: 15 September 2019
Accepted: 11 December 2019
Published: 28 January 2020

Citation:
Liu X, Fu J, Zhao D, Hao Y, Zhu H, Xu M, Zhang B, Jie W and Xu Y (2020) $MAPbBr_{3-x}I_x$ Crystals Improved by Accurate Solution-Grown Procedure for Alpha Particle Detection. Front. Phys. 7:232. doi: 10.3389/fphy.2019.00232

High-quality organic–inorganic halide perovskite brings an opportunity for ideal nuclear radiation detection due to its large carrier mobility, lifetime, and heavy atoms. However, the relatively low bulk resistivity restricts its development for alpha particles and X/γ-ray detectors. Here, we report on the $MAPbBr_{3-x}I_x$ (MPB:I) perovskite crystals grown using the modified inverse temperature crystallization method. Based on the measured supersolubility and solubility curves, the heating procedure was accurately designed to control the nucleation and growth rate. The resulting MPB:I single crystals exhibit higher bulk resistivity of 1.4×10^9 Ω cm, which is 10 times that obtained from the traditional inverse temperature crystallization method. Finally, an uncollimated 0.8 μCi ^{241}Am @5.48 MeV alpha particles source was adopted to evaluate the MPB:I single crystals at room temperature condition. The electron mobility (μ_e) and mobility-lifetime product $(\mu\tau)_e$ of (264.6 ± 6.5) cm^2 V^{-1} s^{-1} and $(2.6 \pm 0.3) \times 10^{-3}$ cm^2/V, respectively, were obtained.

Keywords: perovsikte, solution grown crystals, alpha particle detection, $MAPbBr_{3-x}I_x$, modified inverse temperature crystallization method

INTRODUCTION

Semiconducting nuclear detectors have attracted many interests to achieve the higher spatial and energy resolution due to the direct photoelectric conversion [1]. Hybrid metal halide perovskites, a new type of semiconductor material, have shown great competitive in photovoltaic and photoelectric application field because of the chemically robust, low trap density [2, 3], long carrier lifetime [2, 4, 5], and excellent charge transport performance [6]. Thus, both polycrystalline and single-crystalline perovskites have been used for photodetectors [7, 8], X-ray detectors [9–11], and solar cells [12–15].

Although organic–inorganic halide perovskites $MAPbBr_3$ (MPB) single crystals (SCs) has been proven to be a sensitive material for X-ray radiation detectors, the detection performance is still restricted by its large leakage current [16, 17]. Low bulk resistivity is significantly affected by the types and concentrations of defects in MPB SCs, which is mainly determined by the crystal growth. Some modified methods have been reported by different research groups, such as the modified antisolvent vapor-assisted crystallization methods [18], settled temperature and controlled antisolvent diffusion system [19], and seed-crystal inverse temperature crystallization (ITC) method [20]. The obtained resistivity of MPB SCs is mostly in the range of 1×10^7-5×10^8 Ω cm, which is still limited for the development of nuclear detectors.

Therefore, currently, further increasing the resistivity is imperative. Huang's group [21] reported that the charge carrier concentration was reduced in the MPB bulk crystal by dopant compensation of chlorine so that the carrier mobility and lifetime have been improved. For I^--doped MPB:I, there are few literatures on the photoelectric performance, especially radiation detection [22, 23].

Here, we report the MPB:I perovskite crystals grown by a modified ITC (MITC) method. The heating rate is controlled accurately based on the obtained solubility and supersolubility curves. Then, the X-ray diffraction (XRD), scanning electron microscopy, and UV–visible–near infrared spectrum measurements are employed for the characterization of the crystal quality. Finally, the photoresponse and charge carrier transport behaviors are evaluated by light-emitting diode light and alpha particles source, respectively.

EXPERIMENTAL

Materials

The original materials, methylamine (CH_3NH_2) aqueous solution (30 wt-% in water), were purchased from Sinopharm Chemical Reagent Co., Ltd, China. Hydrobromide acid (40 wt-% in water) and *N*, *N*-dimethylformamide (DMF, 99.8%) were purchased from Kermel Reagent Ltd, China. Lead bromide ($PbBr_2$, 98%), and lead iodide (PbI_2, 98%) were purchased from Aladdin Reagent Ltd., China. All these original materials were employed directly without any further purification.

Synthesis of MABr

The hydrobromide acid was added into the CH_3NH_2 with the molar ratio of 1:1.2. After chemical reaction and full cooling, the well-mixed solution was evaporated at ∼70°C in the evaporator for ∼6 h to obtain crude white MABr (MA = CH_3NH_3Br) powders. After washing by absolute ethanol (99.8%) and recrystallization in anhydrous diethyl ether (99.0%) for several times, the purified MABr crystalline powders were finally dried in a vacuum oven at 60°C for 24 h.

Crystallization of MPB:I

A MITC method was employed to grow MPB:I single crystals. The MABr, $PbBr_2$, and PbI_2 with the molar ratios of 7:6:1 were dissolved in single solvent DMF for ∼60 min in a magnetic stirring apparatus. The solution concentration was controlled at 1.6, 1.7, 1.8, 1.9, 2.0, and 2.1 M in DMF. After filtering using a 0.22-μm pore size filter membrane, the solution was for standby. To reduce the crystal growth rate of MPB:I, the controlling temperature was increased very slowly at 1–2°C/day and the holding time (∼48 h) for 42, 45, 50, 55, 60, and 65°C, respectively.

Characterization

XRD patterns of MPB:I single crystals were collected using D/Max2500PC with Cu $K_{\alpha 1}$ from 10 to 60° (2θ) under 40 kV tube voltage and 40 mA tube current. Scanning electron microscopy and energy-dispersive spectral maps were measured using a JEOL (JSM-7500F) scanning electron microscope with an Oxford (X-Max50) energy-dispersive spectrometer. UV-VIS-NIR spectrum measurements were performed using a UV–visible spectrophotometry (UV-3150, Shimadzu, Japan). ZHD-300 high-vacuum resistance evaporation coating machine was used for Au electrodes preparation. Current–voltage (I–V) and current–time (I–t) measurements were evaluated using a Keithley 6517b electrometer/high resistance system. The charge transport properties of the MPB:I crystals were evaluated by an uncollimated ^{241}Am @5.48 MeV particle source at room temperature in air. Moreover, an ORTEC 710 high voltage supply, a charge sensitive preamplifier (ORTEC 142), and a shaping amplifier (ORTEC 570) with an optimized shaping time of 2 μs were used during the measurement. Finally, a standard Imdetek AMCA-01 multichannel analyzer was employed for the pulse height spectra acquisition.

RESULTS AND DISCUSSION

Crystal Growth and Structure

Because the priorities of halogen solubility in precursor solution DMF are shown below: I > Br > Cl, the replacement of Br by I can maintain the driving force in nucleation and growth processes under higher supersaturation [22]. The supersolubility was measured by a series of solution under the initial concentrations from 1.6 to 2.1 M (2.1 M cannot be completely dissolved at room temperature). After being sealed completely, two batches of solution were placed in a temperature-controlled water tank, in which the temperature could be controlled with a maximum fluctuation of 0.1°C.

For supersolubility measurement, the solution was heated at a rather low speed (1–2°C/day). In the solution growth process, once we observed tiny crystals the first time, the concentration at this temperature was recognized as the supersolubility. Then, a series of the same concentration solution was chosen for solubility measurement. The solution was kept preserved at a certain constant temperature for a long holding time (∼48 h) to ensure that the crystal growth process is completed. Based on the solute mass (the raw material weight), the initial solution volume, and the weight of crystals, the concentration of solubility at a temperature range from 40 to 65°C was obtained.

Three processing zones (nucleation zone, growth zone, and dissolution zone) were divided by the two curves (supersolubility and solubility curves), as shown in **Figure 1A**. First, in the dissolution zone (Part III), all the raw materials were dissolved in the solution. With the temperature increasing, the solubility of precursors decreases, and the solution enters the nucleation zone (Part I); the tiny crystals began to occur. Then, to avoid the new crystal nucleation, the solution is maintained in the growth zone (Part II).

During the traditional ITC growth, the rapid heating usually leads to higher nucleation rate; thus, the grains are in small sizes because of lots of nucleation. Besides, the larger supersaturation of MPB:I in the precursor solution also results in the fast nucleation. Therefore, the crystal size is limited, and the crystals are usually overlapped, as shown in **Figure 1B**.

To reduce the nucleation and growth rates, the heating process was taken into account. As a result, fewer numbers of MPB:I

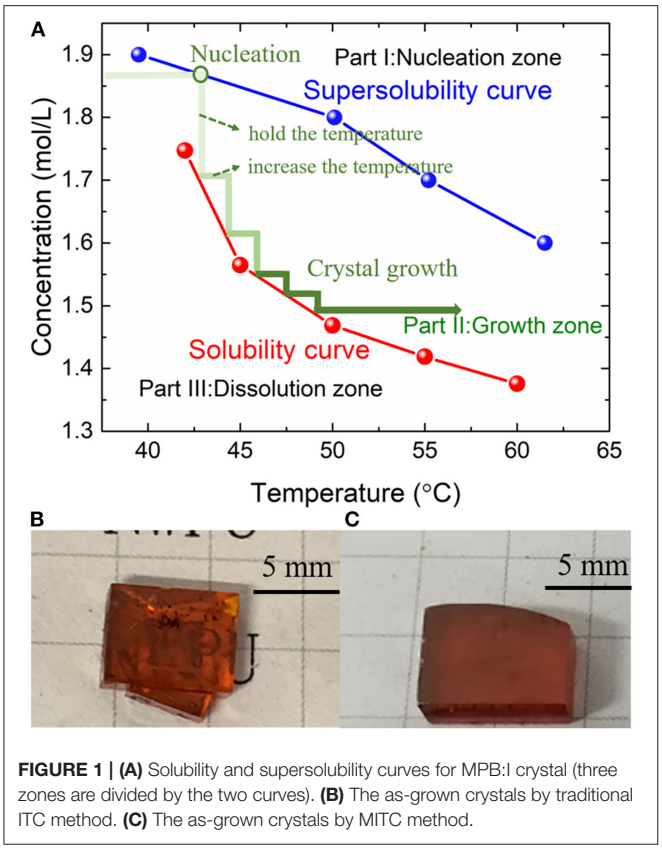

FIGURE 1 | (A) Solubility and supersolubility curves for MPB:I crystal (three zones are divided by the two curves). **(B)** The as-grown crystals by traditional ITC method. **(C)** The as-grown crystals by MITC method.

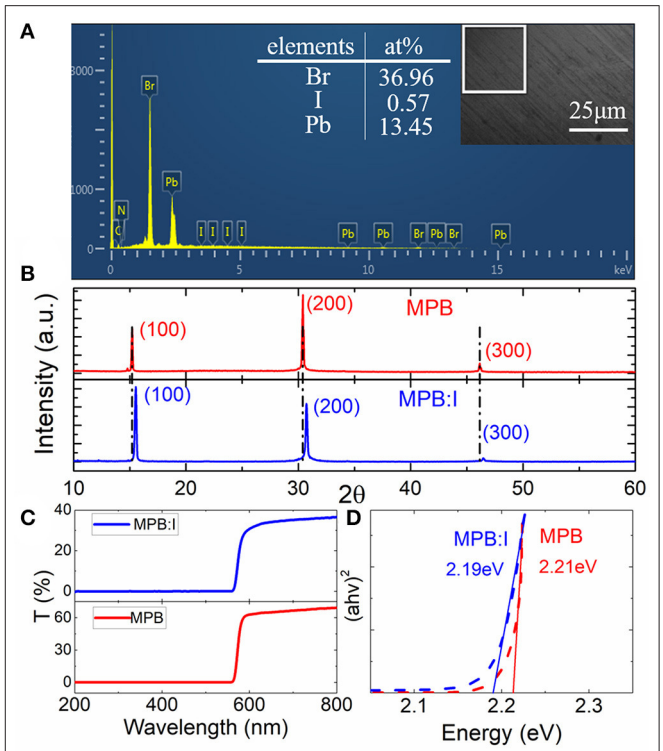

FIGURE 2 | (A) Scanning electron microscopy (SEM) and energy dispersive spectroscopy (EDS) of the MPB:I crystals. The inset picture shows the planar area mapping. **(B)** X-ray diffraction (XRD) patterns with red line for MPB and blue one for MPB:I single crystals. **(C)** The UV-VIS-NIR spectrum of MPB:I and MPB single crystals, respectively. **(D)** The obtained band gap with red line for MPB:I single crystals and blue one for MPB single crystals.

tiny crystals were observed at the beginning of the crystal growth process by the MITC method. After ∼10 days, less than four single crystals were observed in the precursor solution, with the average dimension over 5 × 5 × 2 mm^3 (**Figure 1C**).

The color of MPB:I single crystals is dark red when iodide was introduced, from **Figures 1B,C**. Comparing **Figures 1B**,**C**, surface roughness and crystal morphology are improved by the MITC method, and the stacking-free MPB:I SCs are obtained.

Furthermore, the I content was characterized by energy dispersive spectroscopy, as shown in **Figure 2A**. The obtained ratio of Pb/Br/I is 13.45:36.96:0.57. The resulting value of x in MAPbBr$_{3-x}$I$_x$ is 0.04. According to the molar ratio of the raw materials MABr, PbBr$_2$, and PbI$_2$ (7:6:1), the nominal doping ratio of x in MAPbBr$_{3-x}$I$_x$ is 0.286. The actual I content is lower than the theory value, which may be attributed to the larger ionic radius of iodine [ABX$_3$; ionic radius r_X, 0.22 nm (r_I) > 0.196 nm (r_{Br})], making it hard to enter into the crystal lattice in MAPbBr$_3$ [24].

Figure 2B shows the XRD patterns of the MPB:I and MPB crystals. The sharp peaks in each curve suggest the pure phase of single crystals, without any impurity phase peaks. The (100) peaks of the MPB and MPB:I crystals appeared at 2θ of 15.22 and 15.51°, respectively. Using the equation $d = \lambda/(2\sin\theta)$, the corresponding lattice constants are obtained. Therefore, it clearly suggested that the lattice can be adjusted by the compensation of the doped iodine. Furthermore, the UV-VIS-NIR spectra of the MPB (thickness of 4.64 mm) and MPB:I (thickness of 3.62 mm) were measured from 200 to 800 nm, as shown in **Figure 2C**. Based on the spectrum and Tauc law [25], the bandgaps of the direct-gap semiconductor were obtained, which decreased from 2.21 to ∼2.19 eV, as seen in **Figure 2D**.

Resistivity and Photoresponse

Here, two representative MPB:I crystals were adopted, named MPB:I-1 (traditional ITC method, 5.82 × 5.11 × 3.14 mm^3), MPB:I-2 (modified ITC method, 5.27 × 4.73 × 1.03 mm^3), respectively. Au/MPB:I/Au devices were fabricated by thermal evaporation with thickness of 80 nm Au electrode.

The I–V curves of the above MPB:I single crystals are shown in **Figure 3A**. The resistivity of MPB:I-1 is 1.4 × 10^8 Ω cm. As comparison, the reported resistivity of solution-processed Pb-based perovskite (MPB and MPI) single crystals exhibits a large range from 10^7 to 10^8 Ω cm [26–28]. The resistivity is enhanced by the MITC method, which reaches (1.4 ± 0.02) × 10^9 Ω cm in as-grown MPB:I-2 (as shown in **Figure 3B**).

To investigate the photoresponse performance, the MPB:I-2 crystal was illuminated by a 375-nm light-emitting diode UV light with the power of 14.09 mW/cm^2 at bias range from 1 to 50 V (as shown in **Figure 3C**). In **Figure 3C**, we can find that the values of dark current of 1 and 50 V are 2.4 and 315 nA,

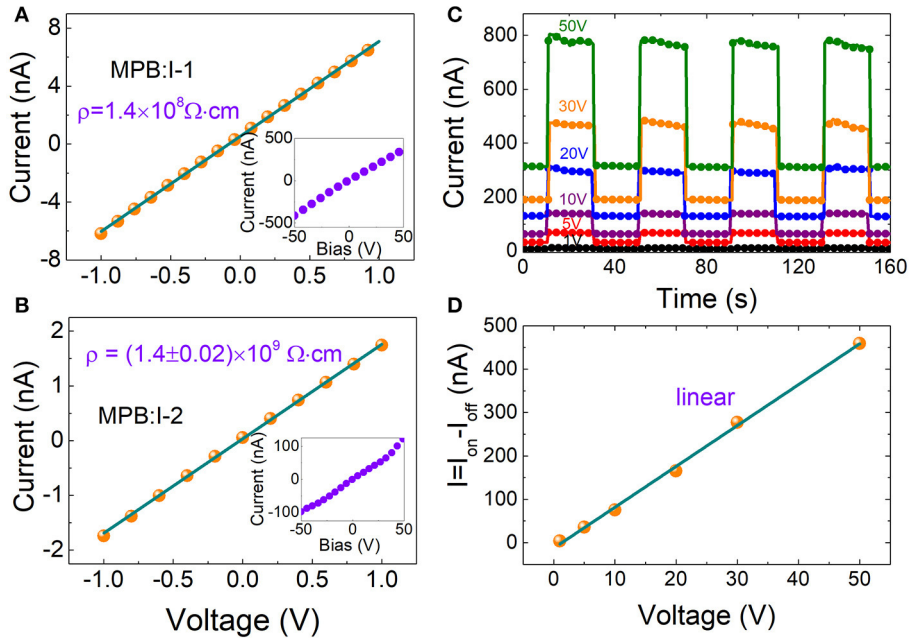

FIGURE 3 | The current–voltage curve from −1 to 1 V for **(A)** MPB:I-1 and **(B)** MPB:I-2. Inset is *I–V* curve from −50 to 50 V. **(C)** Photocurrent of MPB:I-2 under light pulses with 375 nm and 14 mW/cm^2 measured under different biases. **(D)** The current ($I_{on} - I_{off}$) as a function of bias from 1 to 50 V.

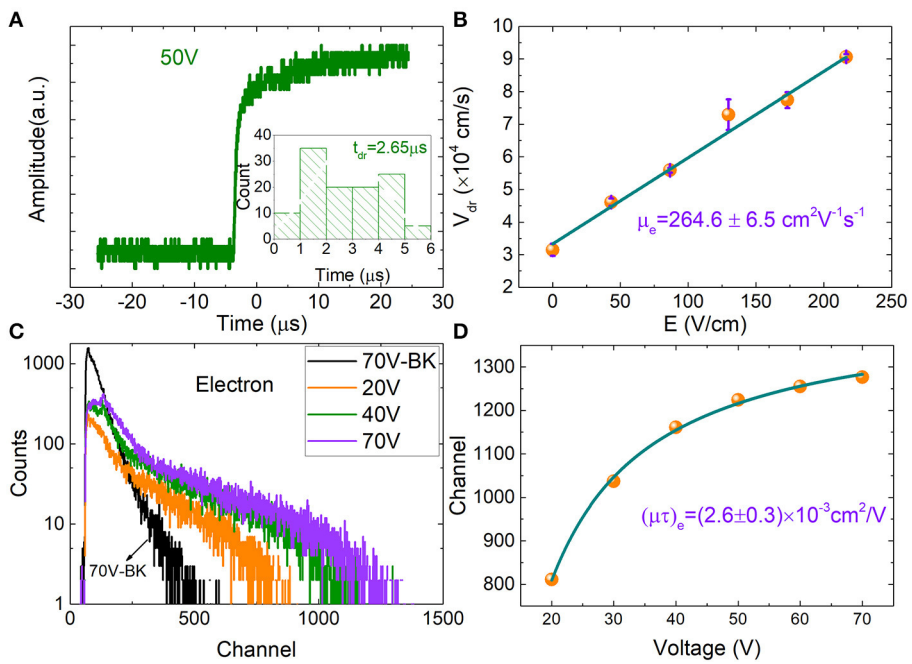

FIGURE 4 | (A) Typical voltage pulses from preamplifier induced by α particles at 50 V bias. The distribution of the pulse rise time (10–90%) under 50 V bias for electrons. **(B)** Electron drift velocity as a function of electrical field strength. **(C)** α Particle pulse height spectra for the MPB:I detector incident on the cathode. **(D)** Fitted using the single-carrier Hecht equation, the electron mobility lifetime product $(\mu\tau)_e$ of MPB:I detector was obtained.

respectively. There are more than 50 times difference between 1 and 50 V. The baseline shift phenomenon appeared as the bias increases. In our past research, the baseline shift phenomenon often happens on current–time curve measurements of 3D Pb-based perovskites samples. Maybe, Br ion migration leads to this problem.

According to the ion-beam-induced charge [29] and photoconductivity [10], the charge collection efficiency is not linear and reaches saturation gradually as the bias voltage increases. However, in this work, the ΔI ($I_{on} - I_{off}$) is linear and not saturated even at bias of 50 V (as shown in **Figure 3D**).

α Particle Detection Characterization

Charge carrier mobility (μ) and mobility-lifetime product ($\mu\tau$) of the MPB:I-2 sample are evaluated by the alpha particles. The measurements were carried out at room temperature and air condition. Generally, the incident depth of the α particles is near the surface of the crystal detector, with the distance of dozens of micrometers (<50 μm) [18, 30]. Therefore, we use the simplified single-carrier approximation Hecht equation (Equation 1) [29] to estimate the electron mobility-lifetime product $(\mu\tau)_e$.

$$\mathrm{CCE} = \frac{\mu\tau U}{d^2}\left(1 - e^{\frac{-d^2}{\mu\tau U}}\right) \quad (1)$$

where U is the applied voltage, and d is the device thickness.

Simultaneously, we used time-of-flight technique to analyze pulse shape rise time and extract the carrier mobility (μ) of MPB:I detector. **Figure 4A** shows the transient pulse for the MPB:I-based detector under 50 V. Generally, a 10–90% amplitude rise time $\tau_{10-90\%}$ was selected for further processing. Through analyzing the pulse height rise time distribution, the carrier drift time (t_{dr}) was acquired. Under the bias from 10 to 50 V, the t_{dr} were 5.01, 4.13, 3.16, 2.98, and 2.65 μs, respectively. The mobility μ is given by

$$\mu = \frac{V_{dr}}{E} = \frac{d^2}{V \times t_{dr}} \quad (2)$$

where V is the bias, t_{dr} is carrier drift time, and d is the thickness of the MPB:I detectors.

The estimated electron mobility (μ_e) for the MPB:I detector is (264.6 ± 6.5) cm^2 V^{-1} s^{-1}, seen in **Figure 4B**, which is higher than the reported μ_e for MPB and MPI single crystals with the value in the range of 24–167 cm^2 V^{-1} s^{-1} [2, 4, 31–35] using the transient photocurrent response measurements. The high mobility of MPB:I may be attributed to the reduction in trap-state density and the charge carrier concentration and inhibition of ionic migration by I-doped compensation.

Figure 4C shows the pulse height spectra vs. applied bias for MPB:I-3 detector, which were illuminated by ^{241}Am alpha particles source. With the applied bias increases, the cutoff edges of the curves reasonably shift to the high channel direction. The electron mobility-lifetime product $(\mu\tau)_e$ is estimated to be (2.6 ± 0.3) × 10^{-3} cm^2/V (**Figure 4D**) by fitting the channel (cutoff edges of the curves) vs. the applied bias using the single-carrier Hecht equation.

CONCLUSIONS

High-resistivity MPB:I bulk crystals have been grown by the MITC method. Both supersolubility and solubility curves were acquired to tailor the growth rate by controlling the heating process. The Au/MPB:I/Au structure device exhibits a higher resistivity of 1.4 × 10^9 Ω cm. The electron mobility-lifetime ($\mu\tau_e$) products are (2.6 ± 0.3) × 10^{-3} cm^2/V by fitting the corresponding pulse height spectra as a function of the applied bias using the Hecht equation. The electron mobility is estimated to be (264.6 ± 6.5) cm^2 V^{-1} s^{-1}, using a 0.8 μCi ^{241}Am α particle source @5.48 MeV measured at room temperature under air environment.

DATA AVAILABILITY STATEMENT

All datasets generated for this study are included in the article/supplementary material.

AUTHOR CONTRIBUTIONS

XL and YX conceived the idea. XL, BZ, and YX designed the experiments. JF and YH synthesized MABr, the perovskite precursors, and crystals growth. MX carried out scanning electron microscopy and EDS measurements. XL and DZ performed the UV-VIS-NIR spectrum measurements, I-V measurements, and I-t measurements. XL and HZ performed alpha particle detection measurements. XL and YX analyzed the data. XL, DZ, and YX drafted the manuscript. BZ, WJ, and YX advised on the overall experiments with critical comments, and finalized the manuscript. All the authors contributed to interpretation of the results and revision of the manuscript.

FUNDING

This work was supported by the National Natural Science Foundations of China (Nos. U1631116, 51872228, and 51802262). This project was also supported by the National Key Research and Development Program of China (2016YFE0115200) and the Natural Science Basic Research Plan in Shaanxi Province of China (2019ZDLGY04-07), the Natural Science Foundation of Shaanxi Province (2019JQ-459), and the Fundamental Research Funds for the Central Universities (3102018jcc036, 3102019TS0408).

REFERENCES

1. Szeles C. CdZnTe and CdTe materials for X-ray and gamma ray radiation detector applications. *Phys Status Solidi B.* (2004) **241**:783–90. doi: 10.1002/pssb.200304296
2. Shi D, Adinolfi V, Comin R, Yuan M, Alarousu E, Buin A, et al. Low trap-state density and long carrier diffusion in organolead trihalide perovskite single crystals. *Science.* (2015) **347**:519–22. doi: 10.1126/science.aaa2725
3. Lian Z, Yan Q, Gao T, Ding J, Lv Q, Ning C, et al. Perovskite $CH_3NH_3PbI_3$ (Cl) single crystals: rapid solution growth, unparalleled crystalline quality,

and low trap density toward 108 cm^{-3}. *J Am Chem Soc.* (2016) **138**:9409–12. doi: 10.1021/jacs.6b05683
4. Dong Q, Fang Y, Shao Y, Mulligan P, Qiu J, Cao L, et al. Electron-hole diffusion lengths> 175 μm in solution-grown $CH_3NH_3PbI_3$ single crystals. *Science.* (2015) **347**:967–70. doi: 10.1126/science.aaa5760
5. Bi Y, Hutter EM, Fang Y, Dong Q, Huang J, Savenije TJ. Charge carrier lifetimes exceeding 15 μs in methylammonium lead iodide single crystals. *J. Phys Chem Lett.* (2016) **7**:923–8. doi: 10.1021/acs.jpclett.6b00269
6. Heo JH, Im SH, Noh JH, Mandal TN, Lim C-S, Chang JA, et al. Efficient inorganic–organic hybrid heterojunction solar cells containing perovskite compound and polymeric hole conductors. *Nat Photonics.* (2013) **7**:486–91. doi: 10.1038/nphoton.2013.80
7. Liu Y, Zhang Y, Zhao K, Yang Z, Feng J, Zhang X, et al. A 1300 mm^2 ultrahigh-performance digital imaging assembly using high-quality perovskite single crystals. *Adv Mater.* (2018) **30**:1707314. doi: 10.1002/adma.201707314
8. Ahmadi M, Wu T, Hu B. A review on organic–inorganic halide perovskite photodetectors: device engineering and fundamental physics. *Adv Mater.* (2017) **29**:1605242. doi: 10.1002/adma.201605242
9. Yakunin S, Sytnyk M, Kriegner D, Shrestha S, Richter M, Matt GJ, et al. Detection of X-ray photons by solution-processed organic-inorganic perovskites. *Nat Photonics.* (2015) **9**:444–9. doi: 10.1038/nphoton.2015.82
10. Pan W, Wu H, Luo J, Deng Z, Ge C, Chen C, et al. $Cs_2AgBiBr_6$ single-crystal X-ray detectors with a low detection limit. *Nat Photonics.* (2017) **11**:726–32. doi: 10.1038/s41566-017-0012-4
11. Panneerselvam DM, Kabir MZ. Evaluation of organic perovskite photoconductors for direct conversion X-ray imaging detectors. *J Mater Sci Mater El.* (2017) **28**:1–8. doi: 10.1007/s10854-017-6409-5
12. Yin W-J, Yang J-H, Kang J, Yan Y, Wei S-H. Halide perovskite materials for solar cells: a theoretical review. *J Mater Chem A.* (2015) **3**:8926–42. doi: 10.1039/C4TA05033A
13. Kim HS, Seo JY, Park NG. Material and device stability in perovskite solar cells. *ChemSusChem.* (2016) **9**:2528–40. doi: 10.1002/cssc.201600915
14. Grancini G, Roldáncarmona C, Zimmermann I, Mosconi E, Lee X, Martineau D, et al. One-year stable perovskite solar cells by 2D/3D interface engineering. *Nat Commun.* (2017) **8**:15684. doi: 10.1038/ncomms15684
15. Yang D, Sano T, Yaguchi Y, Sun H, Sasabe H, Kido J. Achieving 20% efficiency for low-temperature-processed inverted perovskite solar cells. *Adv Funct Mater.* (2018) **29**:1807556. doi: 10.1002/adfm.201807556
16. Onoda-Yamamuro N, Matsuo T, Suga, H. Dielectric study of $CH_3NH_3PbX_3$ (X= Cl, Br, I). *J Phys Chem Solids.* (1992) **53**:935–9. doi: 10.1016/0022-3697(92)90121-S
17. Meloni S, Moehl T, Tress W, Franckevičius M, Saliba M, Lee YH, et al. Ionic polarization-induced current–voltage hysteresis in $CH_3NH_3PbX_3$ perovskite solar cells. *Nat Commun.* (2016) **7**:10334. doi: 10.1038/ncomms10334
18. Liu X, Zhang H, Zhang B, Dong J, Jie W, Xu, Y. Charge transport behavior in solution-grown methylammonium lead tribromide perovskite single crystal using alpha particles. *J Phys Chem C.* (2018) 14355–61. doi: 10.1021/acs.jpcc.8b03512
19. Zhang L, Liu Y, Ye X, Han Q, Ge C, Cui S, et al. Exploring anisotropy on oriented wafers of $MAPbBr_3$ crystals grown by controlled antisolvent diffusion. *Cryst Growth Des.* (2018) **18**:6652–60. doi: 10.1021/acs.cgd.8b00896
20. Huang J, Shao Y, Dong, Q. Organometal trihalide perovskite single crystals: a next wave of materials for 25% efficiency photovoltaics and applications beyond? *J Phys Chem Lett.* (2015) **6**:3218–27. doi: 10.1021/acs.jpclett.5b01419
21. Wei H, Desantis D, Wei W, Deng Y, Guo D, Savenije TJ, et al. Dopant compensation in alloyed $CH_3NH_3PbBr_3$-xClx perovskite single crystals for gamma-ray spectroscopy. *Nat Mater.* (2017) **16**:826–33. doi: 10.1038/nmat4927
22. Wang L, Yuan G, Duan R, Huang F, Wei T, Liu Z, et al. Tunable bandgap in hybrid perovskite $CH_3NH_3Pb(Br_{3-y}X_y)$ single crystals and photodetector applications. *AIP Adv.* (2016) **6**:045115. doi: 10.1063/1.4948312
23. Zhang Y, Liu Y, Li Y, Yang Z, Liu SF. Perovskite $CH_3NH_3Pb(Br_xI_{1-x})_3$ single crystals with controlled composition for fine-tuned bandgap towards optimized optoelectronic applications. *J Mater Chem C.* (2016) **4**:9172–8. doi: 10.1039/C6TC03592B
24. Chonghea L, Xionggang L, Weizhong D, Liming F, Yonghui G, Ziming G. Formability of ABX3 (X = F, Cl, Br, I) halide perovskites. *Acta Crystallogr.* (2008) **64**:702–7. doi: 10.1107/S0108768108032734
25. Tauc J, Menth A. States in the gap. *J Non·Cryst Solids.* (1972) **8**:569–85. doi: 10.1016/0022-3093(72)90194-9
26. Saidaminov MI, Haque MA, Almutlaq J, Sarmah S, Miao XH, Begum R, et al. Inorganic lead halide perovskite single crystals: phase-selective low-temperature growth, carrier transport properties, and self-powered photodetection. *Adv Opt Mater.* (2017) **5**:1600704. doi: 10.1002/adom.201600704
27. Rakita Y, Kedem N, Gupta S, Sadhanala A, Kalchenko V, Böhm ML, et al. Low-temperature solution-grown $CsPbBr_3$ single crystals and their characterization. *Cryst Growth Des.* (2016) **16**:5717–25. doi: 10.1021/acs.cgd.6b00764
28. Dirin DN, Cherniukh I, Yakunin S, Shynkarenko Y, Kovalenko MV. Solution-grown $CsPbBr_3$ perovskite single crystals for photon detection. *Chem Mater.* (2016) **28**:8470–4. doi: 10.1021/acs.chemmater.6b04298
29. Sellin P, Davies A, Gkoumas S, Lohstroh A, Özsan M, Parkin J, et al. Ion beam induced charge imaging of charge transport in CdTe and CdZnTe. *Nucl Instrum Meth B.* (2008) **266**:1300–6. doi: 10.1016/j.nimb.2007.11.074
30. Xu Y, Fu X, Zheng H, He Y, Lin W, McCall KM, et al. Role of stoichiometry in the growth of large $Pb_2P_2Se_6$ crystals for nuclear radiation detection. *ACS Photonics.* (2017) **5**:566–73. doi: 10.1021/acsphotonics.7b01119
31. Saidaminov MI, Abdelhady AL, Murali B, Alarousu E, Burlakov VM, Peng W, et al. High-quality bulk hybrid perovskite single crystals within minutes by inverse temperature crystallization. *Nat Commun.* (2015) **6**:7586. doi: 10.1038/ncomms8586
32. Wenger B, Nayak PK, Wen X, Kesava SV, Noel NK, Snaith HJ. Consolidation of the optoelectronic properties of $CH_3NH_3PbBr_3$ perovskite single crystals. *Nat Commun.* (2017) **8**:590. doi: 10.1038/s41467-017-00567-8
33. Zhao D, Skelton JM, Hu H, La-o-Vorakiat C, Zhu J-X, Marcus RA, et al. Low-frequency optical phonon modes and carrier mobility in the halide perovskite $CH_3NH_3PbBr_3$ using terahertz time-domain spectroscopy. *Appl Phys Lett.* (2017) **111**:201903. doi: 10.1063/1.4993524
34. Wei H, Fang Y, Mulligan P, Chuirazzi W, Fang HH, Wang C, et al. Sensitive X-ray detectors made of methylammonium lead tribromide perovskite single crystals. *Nat Photonics.* (2016) **10**:333–9. doi: 10.1038/nphoton.2016.41
35. Liu Y, Yang Z, Liu, S. Recent progress in single-crystalline perovskite research including crystal preparation, property evaluation, and applications. *Adv Sci.* (2018) **5**:1700471. doi: 10.1002/advs.201700471

Conflict of Interest: The authors declare that the research was conducted in the absence of any commercial or financial relationships that could be construed as a potential conflict of interest.

The handling editor declared a past co-authorship with the authors BZ and YX.

Copyright © 2020 Liu, Fu, Zhao, Hao, Zhu, Xu, Zhang, Jie and Xu. This is an open-access article distributed under the terms of the Creative Commons Attribution License (CC BY). The use, distribution or reproduction in other forums is permitted, provided the original author(s) and the copyright owner(s) are credited and that the original publication in this journal is cited, in accordance with accepted academic practice. No use, distribution or reproduction is permitted which does not comply with these terms.